Elsevier Editorial System(tm) for
International Journal of Fatigue
Manuscript Draft

Manuscript Number:

Title: Multiple Crack Growth Prediction in AA2024-T3 Friction Stir Welded Joints, Including Manufacturing Effects

Article Type: Original Research Paper

Keywords: Friction Stir Welding; Residual Stress; Crack propagation; FEM; DBEM.

Corresponding Author: Dr. pierpaolo carlone, PhD

Corresponding Author's Institution: University of Salerno

First Author: pierpaolo carlone, PhD

Order of Authors: pierpaolo carlone, PhD; Roberto G Citarella, PhD; Mads R Sonne, PhD; Jesper H Hattel, PhD

Manuscript Region of Origin: Europe

Dear Editor,

Please find enclosed our manuscript, "Multiple Crack Growth Prediction in AA2024-T3 Friction Stir Welded Joints, Including Manufacturing Effects" by Pierpaolo Carlone, Roberto Citarella, Mads R. Sonne and Jesper H. Hattel, which we would like to submit for publication as an original research paper in International Journal of Fatigue.

Even if the friction stir welding process of aluminum alloys has been deeply investigated during the past years, a wide usage of this technique in safety critical components requires the careful assessment of the performance of welded structures. In particular, the effect of processing parameters on fatigue behavior of the joint is still subject of a lively debate. The manuscript discusses an effective numerical procedure to simulate multiple crack growth in friction stir welded joints. A FEM model has been implemented to simulate the welding process, including metallurgical aspects and assessing the influence of boundary conditions. Then, FEM output have been inputted in a DBEM environment for the subsequent multiple crack propagation. Numerical data are supported by experimental evidences related to the processing as well as testing phases. Taking into account the relevance of the topic for both the Academic as well as Industrial Communities, we are confident that the paper would appeal to the readership of International Journal of Fatigue.

We confirm that this manuscript has not been published, accepted, or submitted for publication elsewhere. No earlier version of this paper has been presented elsewhere. No other paper has been published using the same data set.

Best Regards,

Pierpaolo Carlone, PhD
Department of Industrial Engineering
University of Salerno

Graphical Abstract

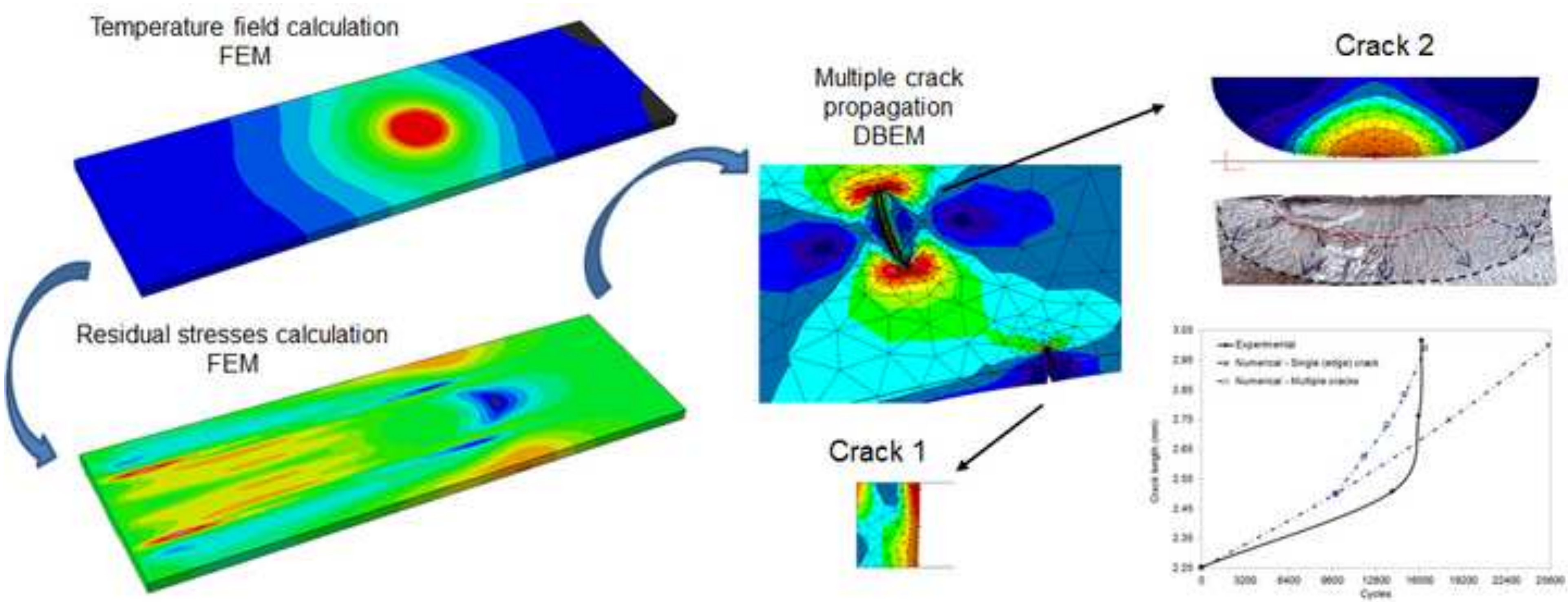

Highlights

1. Multiple crack propagation in FSW joints is simulated by a FEM-DBEM approach.
2. Process induced residual stresses and material softening are predicted by FEA.
3. The significant influence of residual stresses on crack growth is demonstrated.
4. Method predictive capability is evidenced by the numerical-experimental agreement.

Multiple Crack Growth Prediction in AA2024-T3 Friction Stir Welded Joints, Including Manufacturing Effects

Pierpaolo Carlone[1,*], Roberto Citarella[1], Mads R. Sonne[2], Jesper H. Hattel[2]

[1]Department of Industrial Engineering, University of Salerno, Via Giovanni Paolo II 132, 84084, Fisciano, Italy

[2]Department of Mechanical Engineering, Technical University of Denmark, 2800 Kgs. Lyngby, Denmark

*Corresponding author: pcarlone@unisa.it

Abstract

A great deal of attention is currently focused by several industries toward the friction stir welding process to realize lightweight structures. With this aim, the realistic prediction of fatigue behavior of welded assemblies is a key factor. In this work an integrated FEM-DBEM procedure, coupling the welding process simulation to the subsequent crack growth assessment, is proposed and applied to simulate multiple crack propagation, with allowance for manufacturing effects. The friction stir butt welding process of the precipitation hardenable AA2024-T3 alloy was simulated using a thermo-mechanical FEM model to infer the process induced residual stress field and material softening. The computed stress field was transferred to a DBEM environment and superimposed to the stress field produced by a remote fatigue traction load applied on a notched specimen. The whole procedure was finally tested comparing simulation outcomes with experimental data. The good agreement obtained highlights the predictive capability of the method. The influence of the residual stress distribution on crack growth and the mutual interaction between propagating cracks were evidenced as well.

Keywords: Friction Stir Welding, Residual Stress, Crack propagation, FEM, DBEM.

1. Introduction

Friction stir welding (FSW) is a solid state welding technique employed for joining several similar as well as dissimilar materials pairs, generally considered difficult to weld using conventional welding techniques [1-5]. Main benefits provided by FSW over conventional fusion welding processes can be summarized in the reduction of porosity, of microstructure alteration and of process induced residual stresses and distortions. These advantages have made it attractive to several industries, such as aeronautical, automotive, and naval, to cite but a few. Even if several issues concerning microstructure effects and stress-strain development in FSW have already been clarified, a deeper understanding of static and fatigue performances of welded assemblies is imperative for its broader application to structural components. Interesting outcomes on this topic were already discussed in the literature, reporting the slower crack propagation in FSW joint with respect to fusion welded joints. This desirable feature was attributed to microstructure, microhardness, and residual stresses [5-9].

Although residual stresses induced by FSW process are less severe if compared to traditional welding techniques [3,10], they are considered as a major driving force for crack propagation in welded structures. The dominant role of residual stresses on crack growth rates in AA2024 FSW joints was explicitly argued by Bussu and Irving [8]. Their experimental analysis proved also the secondary role played by local microstructure and microhardness. Similar remarks were driven by Fratini et al. in [7]. Dalle Donne et al. warned about the risk of erroneous prediction of crack propagation in FSW joints, if residual stresses effects are not properly accounted for [11]. According to Pouget and Reynolds, accurate growth rates predictions can be achieved including residual stress effects into the calculation, whereas some discrepancies between analytical calculation and experimental outcomes were attributed to microstructure related closure mechanisms, e.g. oxide-induced closure [12]. A completely opposite conclusion was pointed out by Tra et al., who experimentally investigated the role of residual stresses and microstructure on crack propagation in AA6063-T5 FSW joints [13]. They commented that crack propagation is mainly driven by the inhomogeneous microstructure in and around the welded area, whereas the influence of residual stresses is not so significant. It should be noted, however, that an exceptionally low longitudinal residual stress scenario was reported in their work (tensile peak ~ 10 MPa), if compared to similar studies (tensile peak between 60 and 130 MPa).

Recently, some attempts to numerically assess the fatigue behavior in friction stir welded structures were discussed in literature [14-19]. In [15] an approach based on the Boundary Element Method (BEM) was adopted for crack growth simulation. The initial stress scenario was defined generalizing pointwise experimental measurements. The residual stress relaxation phenomenon was taken into account and a variable calibration for the crack growth law was provided depending upon the FSW regimes. The same numerical method was employed by some of the authors of the present work to simulate crack propagation in FSW joints, whereas the usage of Dual Boundary Element Method for crack propagation was preferred to other numerical methods to speed up the remeshing process when considering mixed mode problems. In those papers, experimentally measured longitudinal residual stress distributions in the cross section were assumed as initial condition [16-19]. However, the intrinsic difficulties to experimentally obtain all the components of the residual stress tensor as well as to the lack of generality such hybrid approach significantly reduce its potential application.

In this paper a numerical investigation on the influence of residual stresses, induced by the friction stir welding process, on fatigue crack growth in aluminum friction stir welded butt joints has been proposed. Due to its wide structural application in the aeronautic and aerospace industries, aluminum alloy AA2024, in the T3 ageing condition, was selected as base material. The computational approach is based on the coupled usage of finite element method (FEM) and Dual Boundary Element Method (DBEM). In particular, the thermo-mechanical FEM model, proposed by Sonne et al. in [20], was used to predict the residual stress state in the butt-welded aluminum plates. The computed residual stress field was then superimposed to the stress field produced by a remote fatigue traction load and multiple crack propagation was simulated by the DBEM in an automatic way. The effect of residual stresses on crack growth rates was modeled by the crack growth law adopted in [16-19]. Experimental data were used to validate both FEM and DBEM calculations.

2. FEM-DBEM Model

2.1. Thermo-mechanical FEM model

In thermo-mechanical modelling of FSW, the most convenient and common assumption, used to reduce the computational complexity of the problem, is to neglect the material flow during welding. This results in semi-coupled thermo-mechanical models in a Lagrangian frame, where the thermal field is calculated prior to the mechanical field by separating the two analyses. The model applied in this work was proposed by Sonne et al. [20]. The theoretical basis of this model is briefly explained in this section.

The transient temperature distribution was inferred solving the following energy balance

$$\rho c_p \frac{\partial T}{\partial t} = \frac{\partial T}{\partial x}\left(k\frac{\partial T}{\partial x}\right) + \frac{\partial T}{\partial y}\left(k\frac{\partial T}{\partial y}\right) + \frac{\partial T}{\partial z}\left(k\frac{\partial T}{\partial z}\right) + \dot{Q}'''_{gen} \tag{1}$$

where ρ is the material density, c_p is the specific heat capacity, T is the temperature, k is the thermal conductivity and $\dot{Q}'''_{gen}$ is the volumetric heat source term. The tool action was modelled by means of a suitable boundary condition applied at the interface between the shoulder and the work piece. A surface heat flux, dependent on the radial position and the local (temperature dependent) yield stress, was imposed at the tool shoulder-adjoining material contact area, without modelling the tool probe [21].

The microstructural evolution of the Al-alloys 2024 in the T3 temper state during FSW has been shown to have a significant effect on the residual stress distribution [20]. In this study, the softening model developed by Myhr and Grong [22] was used to predict the phase transformation during welding. The same approach was also adopted by Richards et al. in [23]. The model relates the fraction of dissolved hardening precipitates X_d to the equivalent time of heat treatment, $t_{eq} = t/t^*$ (where t is the period of time at a temperature T and t^* is the time for total precipitate dissolution at this temperature) as follows:

$$\frac{f}{f_0} = 1 - X_d = 1 - t_{eq}^n = 1 - \sqrt{t_{eq}} \tag{2}$$

$$t_{eq} = \sum_{i=1}^{N_{total}} \frac{\Delta t_i}{t_i^*} = \sum_{i=1}^{N_{total}} \frac{\Delta t_i}{t_{ref} exp\left[\frac{Q_{eff}}{R}\left(\frac{1}{T_i} - \frac{1}{T_{ref}}\right)\right]} \tag{3}$$

where t_{ref} is the time for total dissolution at the reference temperature T_{ref}, R is the universal gas constant and Q_{eff} is the effective energy for precipitate dissolution. The fraction of hardening precipitates f/f_0 then relates to the equivalent time t_{eq} via the fraction of dissolved precipitates X_d as shown in Eq. (2), where n is a material constant which is obtained experimentally. A value equal to 0.5 is often used, as indicated in the last part of Eq. (2). The yield stress was then predicted via a linear interpolation between original state and the fully dissolved state.

For calculation of the transient as well as the residual stress field in the work piece, a standard mechanical model based on the solution of the three static force equilibrium equations is used, i.e.

$$\sigma_{ij,j} + p_j = 0 \tag{4}$$

being p_j the body force at any point within the plate and σ_{ij} the stress tensor. Hooke's law and linear decomposition of the strain tensor, as well as small strain theory, were applied together with the expression for the thermal strain. The plastic strain evolution is based on the standard J_2 flow theory with a temperature dependent von Mises yield surface. According to [20], isotropic hardening behavior is the most suitable for modeling the mechanical behavior of AA2024-T3 when combined with a softening model. The yield stress at the instantaneous temperature was found by interpolation between the upper and lower bound yield stress curves in proportion to X_d, as follows:

$$\sigma_y = \left(\sigma_{y_{max}} - \sigma_{y_{min}}\right)\frac{f}{f_0} + \sigma_{y_{min}} \tag{5}$$

being σ_{max} the yield stress of the material in the original T3 condition and σ_{min} the yield stress of the fully dissolved material. The upper and lower yield stress curves for AA2024-T3 are available in [20]. Microhardness distribution was inferred adopting the same model as in Eq. (5), obviously replacing yield stress with microhardness values.

2.2. DBEM crack propagation model

Residual stresses affect crack propagation since they change the effective value of the total Stress Intensity Factor (SIF) at the crack tip, with both the minimum (K_{min}) and the maximum (K_{max}) SIF values generally affected in the same way, so as to leave unchanged the parameter $\Delta K=K_{max}-K_{min}$. Consequently, the primary effects of residual stresses on crack growth rates are related to the K_{max} variations rather than to the ΔK variations. This is accounted for by a two-parameter approach, as detailed in [24,25]. According to this theory, fatigue crack growth is driven by two driving forces, K_{max} and ΔK, whereas the latter term is affected by the applied remote load. In addition, the theory assumes that there are two fatigue thresholds, $K^*_{max,th}$ and ΔK^*_{th} corresponding to the two driving forces: both the driving forces must be simultaneously larger than the relative thresholds for fatigue crack growth to occur. The crack growth law was assumed as follows [24,25]:

$$\frac{da}{dN} = A(\Delta K - \Delta K^*_{th})^n \left(K_{max} - K^*_{max,th}\right)^m \tag{6}$$

In the present work, Eq (6) was calibrated by best fitting the material parameters A, n, m based on literature data [16-19, 25]. Used parameters were defined as follows: ΔK^*_{th} = 1834121 N/m$^{3/2}$,

$K^*_{max,th}$ = 3352014 N/m$^{3/2}$, A = 6.745E-23 m$^{1.5*(n+m)+1}$/N^{n+m}, n = 1.65, m = 0.56. These parameters are valid for each positive R-ratio ($\sigma_{min}/\sigma_{max} > 0$).

Friction stir welding effects were reproduced by taking into account the residual stress influence on the driving parameters ΔK and K_{max}. Namely, SIFs used in Eq. (6) were computed as the sum of the SIF corresponding to the remote load and of the SIF corresponding to process induced residual stresses. Residual stresses were modelled, in the DBEM analysis, by a distribution of tractions applied on the crack faces.

3. Results and discussion

3.1. Welding setup and model validation

In this paragraph, the capability of the implemented model to predict the mechanical properties variation and the residual stresses induced by the welding process is assessed by comparison with experimental data. AA2024-T3 aluminum rolled sheets were joined by FSW using a non-consumable Cr-Mo steel tool, adopting an angular tool velocity equal to 1400 rpm and a welding speed equal to 70 mm/min. Tool geometry was characterized by a flat shoulder (20 mm diameter) with an unthreaded conical pin (6.2 mm major diameter, 30° cone angle, 3.8 mm length). The forging action of the tool shoulder was enhanced imposing a tilt angle of 2°. Dimensions of the adjoining sheets were 200 mm (length), 30 mm (width), and 4 mm (thickness). In Fig. 1 the welding setup is shown. The residual stress scenario used for numerical calculations was computed reproducing the same processing conditions.

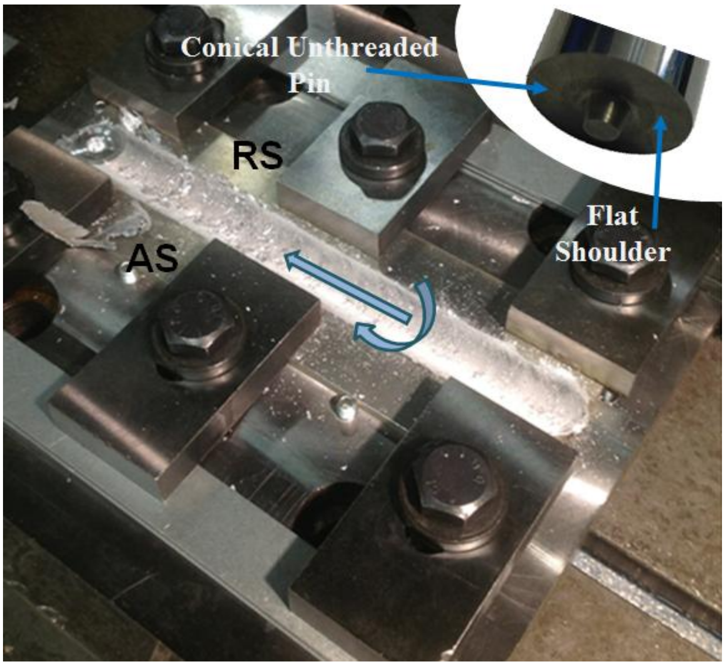

Fig. 1: Welding setup.

For an effective thermo-mechanical modeling it is very important to get a realistic description of the temperature fields from the heat transfer analysis before the subsequent mechanical analysis. Indeed, temperature gradients are both the direct and indirect sources for stresses because of thermal expansion and metallurgical changes in the aluminum, respectively. Please note that the validation of the temperature calculation procedure was provided elsewhere [26] and is not herein repeated in the interest of brevity. The transient temperature field during welding (Fig. 2a), provided by the thermal calculation, was then inputted in the subsequent stress analysis to infer the stress state evolution in the welded plate (Fig. 2b). In Fig. 2b some lines in compression in front of the moving heat source and in tension behind the moving heat source can be observed as a result of the self-constraining effect played by the colder surrounding material.

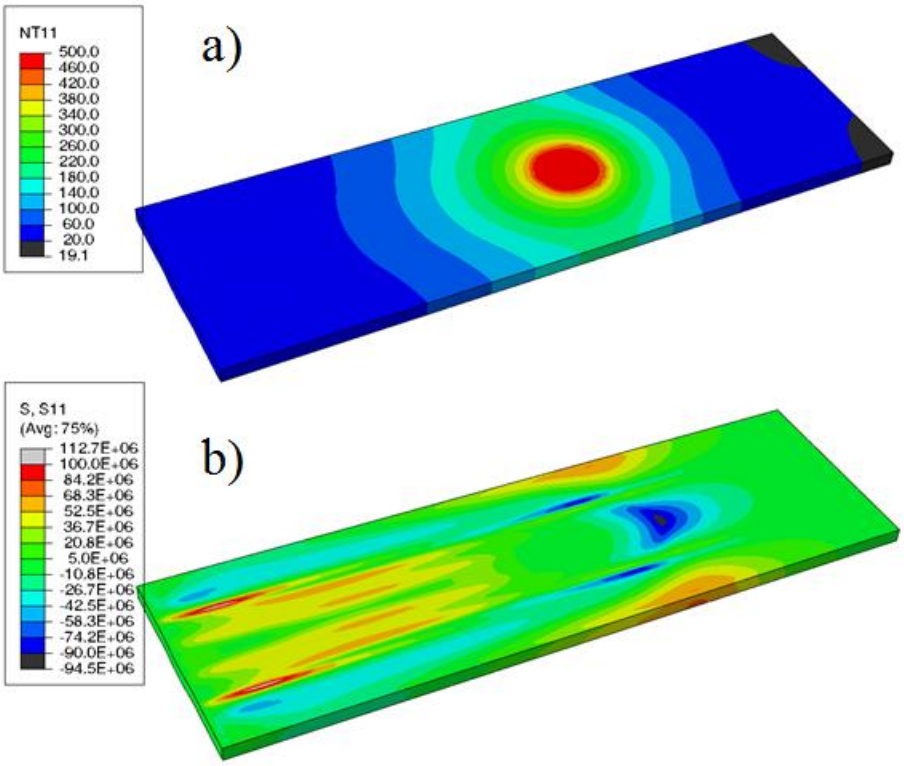

Fig. 2. a) Temperature field (°C) from the heat transfer analysis of welding at t=100 s. b) The resulting longitudinal stress component (N/m^2) from the stress analysis at the same time step.

In the FSW process, heat is generated by the friction between the tool shoulder and the work piece surface, and by the plastic deformation induced in the work piece. The material under the tool is heated up with consequent expansion; however it is partly constrained by the relatively colder material surrounding this region. Subsequently, the material starts yielding in compression and plastic deformation starts to develop. This fundamental mechanism of residual stresses evolution is very similar in all kinds of welding techniques whether are them fusion or solid state welding. Besides, the thermal gradients due to non-uniform heat generation and the mechanical boundary conditions (i.e. clamping, contact conditions between work piece and the anvil, etc.) also plays a significant role for promoting plastic strains and consequent residual stresses [27,28].

The influence of the boundary conditions applied model the clamping system was assessed considering different constraining schemes, ranging from a rigid clamping (out of plane displacements completely constrained in correspondence of the plate-clamp contact areas) to a no clamping condition (preventing only rigid body motion of the model). In between this two extreme cases, an intermediate approach was also explored, based on the consideration of the intrinsic elastic behavior of the clamping bolts as well as of the axial thermal expansion (caused by conductive heat fluxes and heating) experienced by the bolts themselves during the welding process. In particular, spring elements, aligned along the out of plane direction, were connected to nodes belonging to the virtual plate-clamp contact area to reflect the expected reaction of the clamping system.

Numerical outcomes were compared with experimental data to identify the most suitable modelling approach. In particular, the longitudinal residual stresses distribution in the generic transverse cross section of the joint was inferred by means of the contour method [29]. The adopted procedure is fully detailed in [30]. The computed stress field was already used for crack propagation assessment by some of the present authors in [16-19,25], assuming the repetition of an identical stress scenario (as computed at the mid-length) in each cross section orthogonal to the weld line. However, the hybrid (numerical-experimental) method discussed therein is obviously quite expensive and not generalizable, since the stress analysis is case specific, imposing the repetition of the procedure for each variation of processing parameters and conditions. What is more, allowance for transient effects and stress relaxation in proximity of the free edges of the sheets was not provided in the crack growth simulations.

When comparing the measured and simulated longitudinal residual stresses, the well-known M-shape can be observed (see Fig. 3), meaning that the stresses are lower close to the weld centerline than the outer shoulder radius of the tool, irrespective of the applied boundary conditions. However, numerical results highlighted that relaxing the mechanical constraints (no clamping case) implied a significant reduction of the computed tensile peaks (approximately 30% with respect to the experimental value). Accordingly, the compression state moving away from the weld line decreased, in absolute value, to enforce the equilibrium condition on the cross section. On the other hand, some singularities in the longitudinal residual stress profile were detected when excessively severe boundary conditions were applied (rigid clamping case). Indeed, the hard constraining of the out of plane displacements of nodes belonging to the virtual plate-clamp contact area enhanced the compression state at the edges of the plates as well as the tensile state in the tool region, providing a better agreement with experimental data. Nevertheless, unrealistic stress plateaus were introduced in the stress profile at the end of the plate-clamp contact area (± 20 mm from the weld line), due to the abrupt variation in degree of freedom constraining. Reliable predictions were provided using spring elements instead of hard constraining, whereas element stiffness K (2E6 N/mm) was calibrated avoiding unrealistic plateaus as well as flat shapes at the extremities of the profile, as obtained assuming, for instance, K = 10 N/mm (Fig. 3). The residual stresses distribution computed introducing spring elements with K = 2E6 N/mm were used for the crack propagation analysis.

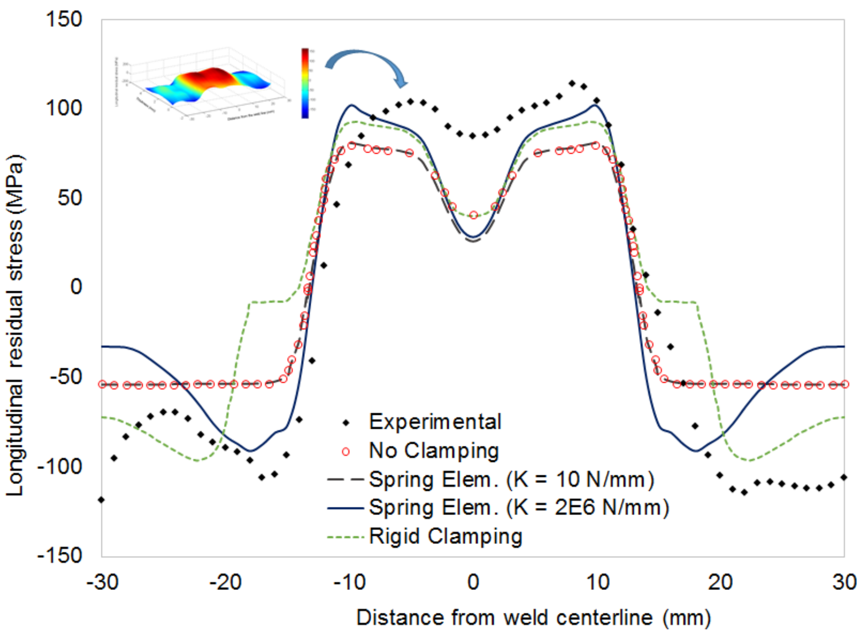

Fig. 3. Comparison of numerical and experimental longitudinal residual stresses.

The sensitivity of calculation results against material properties variations was assessed comparing the numerically estimated and experimentally measured microhardness along a linear pattern orthogonal to the weld line at the mid-thickness of the specimen. Vickers microhardness was measured using an automatic device (LEICA VMHT AUTO) according to the following testing parameters: indentation load 100 gf (0.98 N), loading time 15 s, and indentation speed 60 μm/s. The distance between two consecutive indentations was defined as 1 mm. The analysis was performed after 60 days of (post welding) natural ageing to ensure the establishment of a stable microstructure. Microhardness profiles are compared in Figure 4.

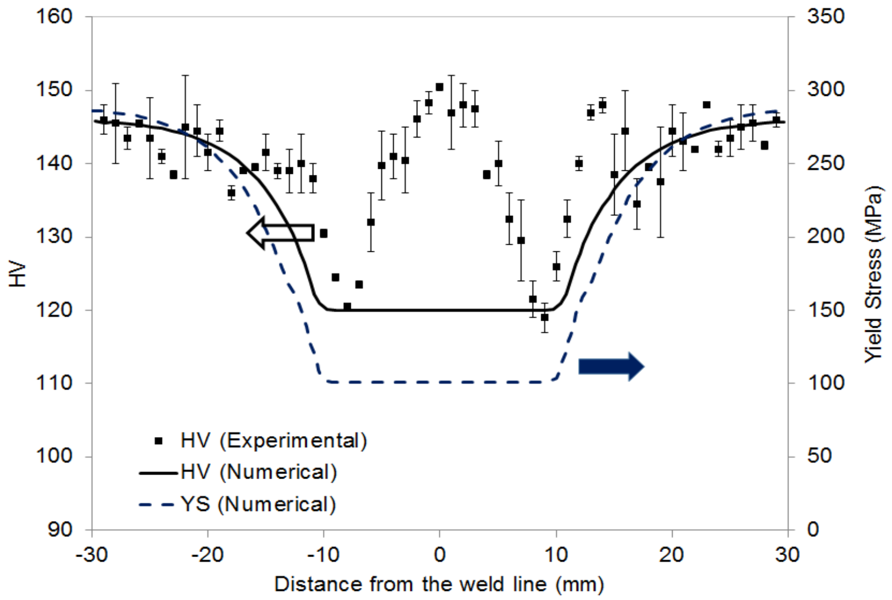

Fig. 4. Micro hardness (numerical and experimental) and yield stress (numerical) profiles

As can be seen, satisfactory agreement between numerical and experimental hardness profiles was achieved in most of the plate, being the main difference localized into the nugget zone, e.g. in correspondence of the weld line. This can be easily explained taking into account that grain refinement and particle re-precipitation, which are the main mechanisms promoting the enhancement of mechanical properties in the considered case, are not included into the simulation of the process. Due to the aforementioned phenomena, a certain hardness recovery is expected when approaching the weld line. At the same location, a similar trend for the yield stress is naturally expected as well.

3.2 Crack propagation

Crack propagation tests were performed using a universal testing machine INSTRON 8502 with a load cell range equal to 250 kN. A fatigue load P_{max} = 24 kN, corresponding to a remote stress σ = 100MPa, was applied with a frequency equal to 10 Hz and a load ratio R = 0.1. In order to predefine the crack initiation site, an initial edge notch with a length equal to 2 mm was realized by wire electro-discharge machining (WEDM) on the retreating side of the weld, at the middle length of the specimen [18]. Two crack gages were applied on both sides of the notch in order to automatically monitor the advancing crack. Experimental tests pointed out a multiple crack propagation scenario, characterized by the presence of the aforementioned lateral crack (crack 1), artificially introduced after the welding process by WEDM and of a central semi-elliptic crack (crack 2), spontaneously nucleated in correspondence of the weld crown due to the surface beach marks left by the tool shoulder.

The residual stresses, stored in the ABAQUS .odb result file, were imported in the commercial suite BEASY [31] for the DBEM crack propagation analysis. The basic hypothesis, to be verified by the simulations, is that, in an initial phase of fatigue test, the central crack, due to its reduced size and to the distance from the lateral crack, does not significantly influence the propagation of the lateral crack itself, whereas, in a second phase, when the central crack depth become comparable to the specimen thickness, the interaction between the two cracks turn out to be non-negligible, with the consequent need for an explicit numerical modelling of a multiple crack scenario.

In particular, in the experiments reported in [18], the lateral crack, starting from the notch tip, was considered initiated when getting a length equal to 0.25 mm (pre-cracking phase); consequently the initial single crack simulated scenario was based on a lateral through crack whose overall length (2.25 mm) was equal to the sum of notch length (2 mm) and pre-crack length (0.25 mm) (Fig. 5). Taking into account that the nucleation time and size for the central crack were not known a priori and considering the absence of experimental evidences indicating, up to this stage, a relevant interaction between the two cracks, the central crack was considered sufficiently small and consequently not modelled at all (Fig. 5).

Then, the lateral crack was extended in single crack propagation simulation, up to 2.5 mm length, before to introduce the second central crack in the model. The timing for the introduction of the central crack in the numerical model was dictated by the following experimental outcomes: when the experimental lateral crack reached 2.5 mm length, underwent a sudden acceleration, experimentally detected and displayed by the applied crack gauges (Fig. 6) [18]; such behaviour was due to the enhanced interaction with the central crack that at this stage has reached appreciable sizes (such results is indirectly suggested by the behaviour of the monitored lateral crack). In particular, the initial lateral crack took nearly 10000 simulated fatigue cycles to increase its length from 2.25 to 2.5 mm (Fig. 6), when the central crack was postulated to initiate, and therefore included in a multiple crack propagation simulation. The position and shape of such (macroscopic) central crack was suggested by the experimental outcomes of a post-mortem inspection of the fracture surface, as shown in Fig. 7. The correctness of such choice will be provided by the satisfactory matching between numerical and experimental final scenario, but can be a priori justified because the lateral crack alone would had continued its numerical propagation with much lower crack growth rates than exhibited experimentally, as shown in Fig. 6. Namely, the thumbnail crack propagation was responsible for such a sharp acceleration on the lateral crack growth rates exhibited in the numerical simulation and this was consistent with experimental outcomes (Fig. 6).

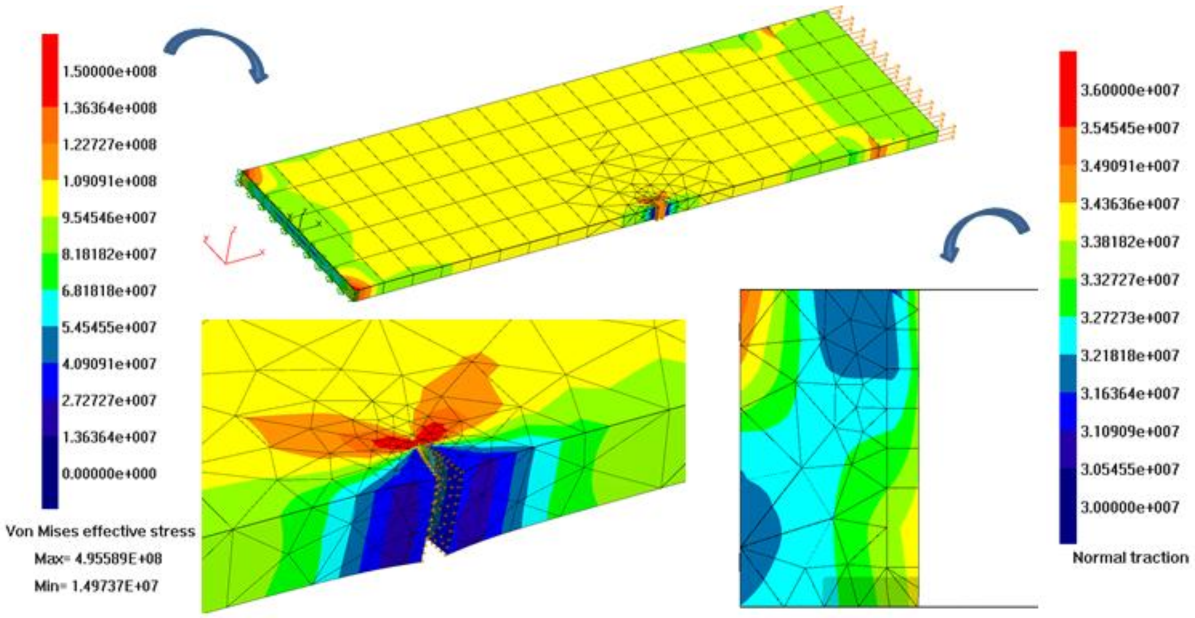

Fig. 5. DBEM initial single crack configuration with highlight of Von Mises stresses (Pa) and normal tractions (Pa) on crack faces (deformation scale = 100).

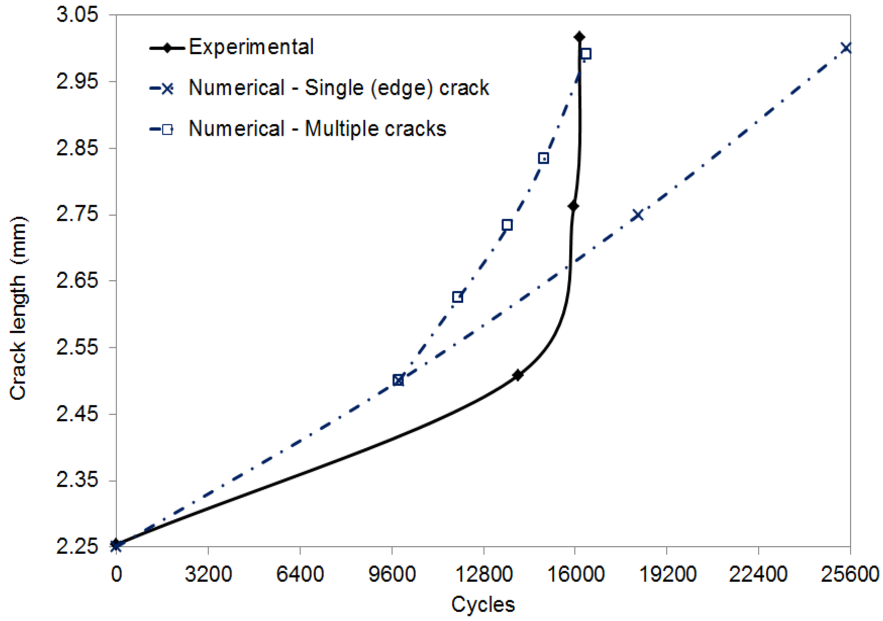

Fig. 6. Lateral crack length, as experimentally monitored and calculated by DBEM, assuming single (lateral) crack propagation (with no central crack), and multiple crack propagation (considering the introduction of an additional central crack after almost 10000 cycles).

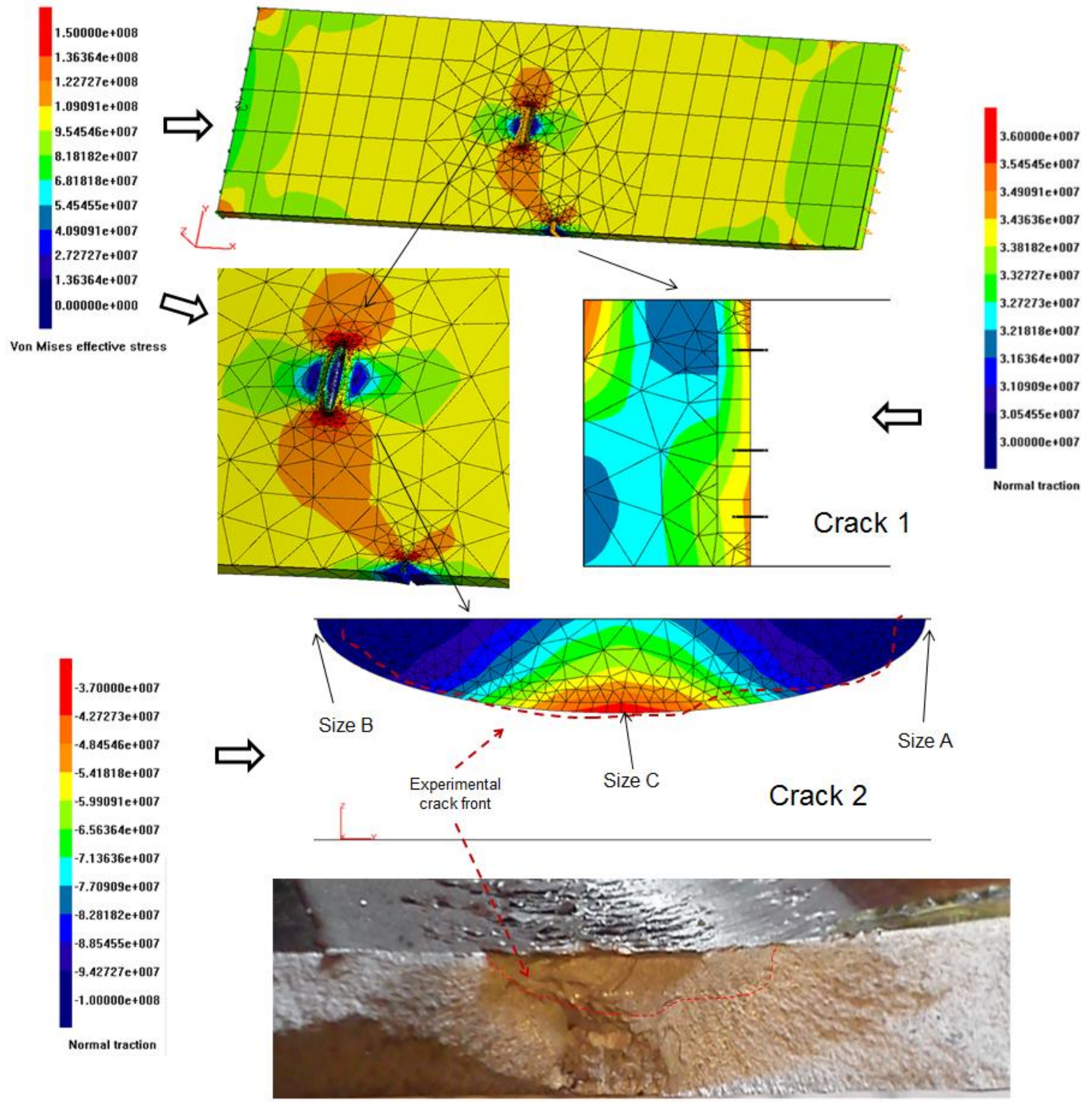

Fig. 7. DBEM initial multiple crack configuration with highlight of Von Mises stresses (Pa), sizing points (A, B, C) along the crack front, normal tractions (Pa) on crack faces (deformation scale = 100), and experimental front at central crack initiation (dashed red line).

After nearly 6550 cycles of multiple crack propagation, subdivided in four crack growth increments, the lateral and central crack reached the sizes showed in Figs. 6 and the thumbnail crack broke through the thickness (Fig. 8), causing the specimen failure for fracture instability. As a matter of fact, considering the yield stress profile depicted in Fig. 4, the residual ligament was still not affected by extensive plastic deformation (Fig. 8), excluding the occurrence of a failure due to plastic collapse. The thumbnail crack became through the thickness with a symmetric advance (Fig. 8) on both the advancing and retreating sides, consistently with the symmetrically distributed residual stresses.

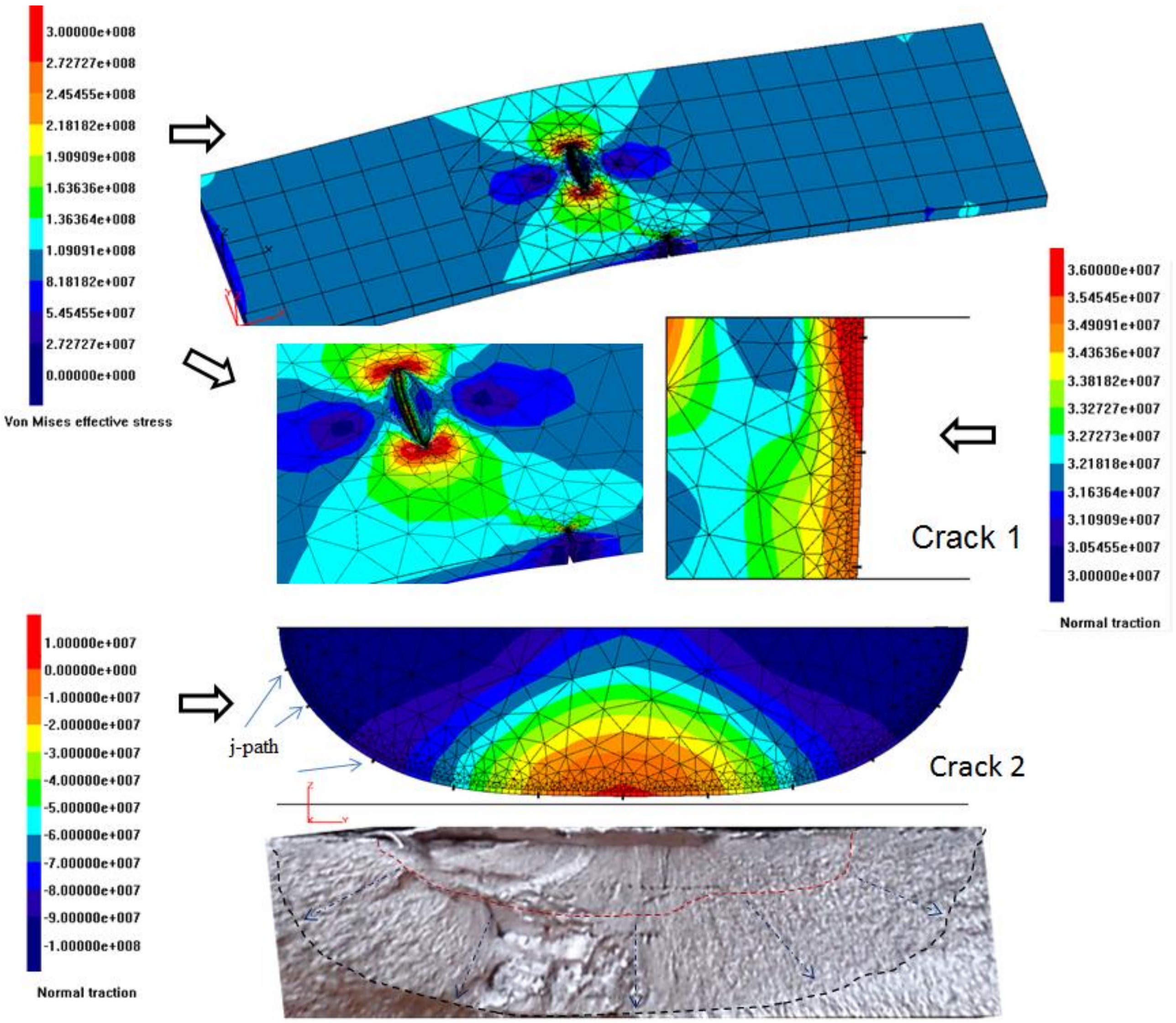

Fig. 8. DBEM final multiple crack configuration with highlight of: Von Mises stresses (Pa), j-path along the crack front, normal tractions (Pa) on crack faces (deformation scale equal to 50), and cross comparison between the last numerical central crack scenario and the specimen failure section (the red and black lines evidence, respectively, the initial modelled crack front and the crack configuration on the verge of ductile rupture).

The central crack propagation turned out to be responsible for specimen failure, with related K_I values (mode II and III are almost negligible) approaching the material fracture toughness [19] (as soon as the crack break through the thickness a further sharp increase of SIFs along the crack front is expected). On the contrary, SIFs along the lateral crack front, as computed using the J-integral approach [32], were not sufficiently higher than threshold (K_{maxth}=3352014 Pa*m$^{0.5}$) to produce appreciable crack advances (Fig. 9).

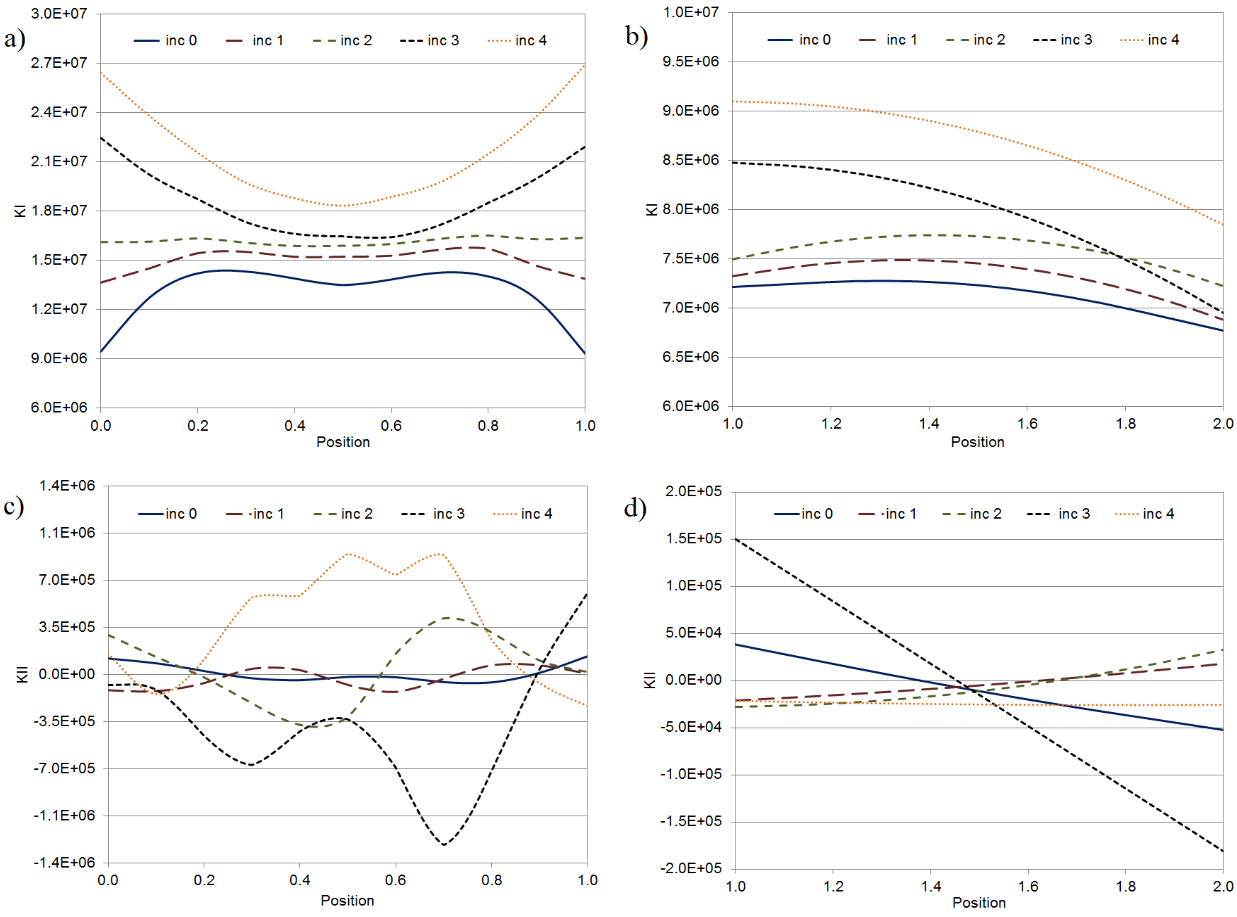

Fig. 9. SIF values (Pa*m$^{0.5}$) along the crack fronts of the two cracks for each simulation increment (inc 0 ~ 9850 cycles; inc 1 ~ 11920 cycles; inc 2 ~ 13660 cycles; inc 3 ~ 14920 cycles; inc 4 ~ 16400 cycles;) of crack propagation: curvilinear abscissa from 0 to 1 refers to crack 2 (subfigures a and c); curvilinear abscissa from 1 to 2 refers to crack 1 (subfigures b and d).

The final numerical central crack configuration (Fig. 8) was consistent with the experimental crack scenario at instability [18]. The final crack front exhibited an elliptical shape (as driven by the residual stresses across the thickness) with a length of the major axis equal to nearly 15.6 mm (Fig. 10). The specimen failure was forecasted after nearly 9850+6550=16400 cycles of crack propagation and the central thumbnail crack started to interact with the lateral crack after 355000-16400=338600 cycles; nearly the same estimate was provided in [18] following a different approach.

It is interesting to observe that by a combined use of simulations and available crack gauge recordings it was possible to circumvent the drawback coming from the lack of crack gauge measurements referred to the central crack. Namely, it was possible to assess the size, after a given number of fatigue cycles, of the crack in the middle of weld even if no direct measurement is available (because there was no expectation of an initiation in that point before to start the test and consequently no crack gauges were applied in that area).

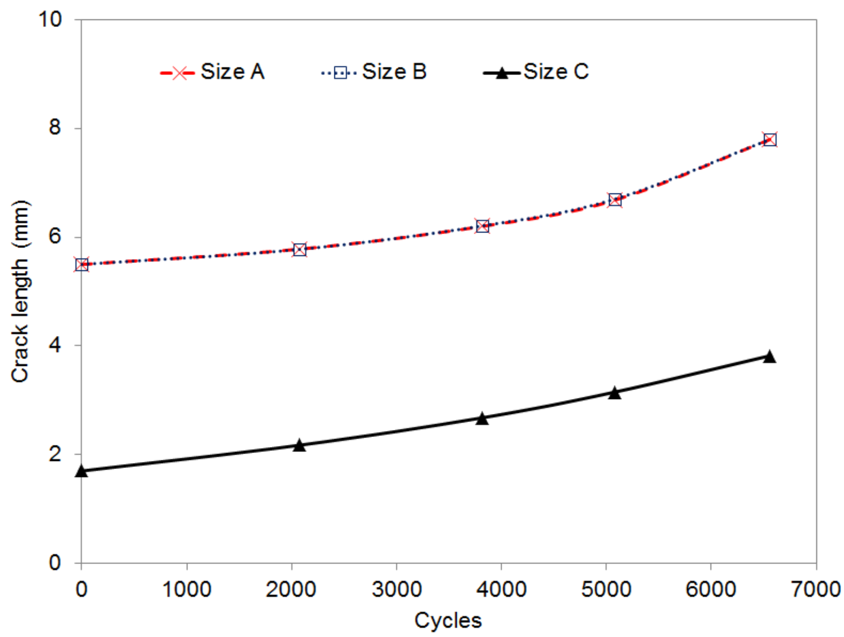

Fig. 10. Crack sizes (mm) for the thumbnail crack (measured at the size points A, B, C) vs. number of cycles.

4. Conclusions

The following conclusions can be highlighted:

– the implemented FEM-DBEM approach proved to be able to effectively predict multiple crack growth in presence of residual stresses induced by the manufacturing process;

– the crack propagation provided by the experimental test, as devised by post mortem metallographic analyses, characterized by nearly pure mode I evolution and nearly symmetric shape (with respect to the weld line mid plane), qualitatively confirmed the residual stress scenario calculated by numerical simulation;

– if the initial crack starts from the weld line the process induced opening stresses play an accelerating effect on the crack propagation;

– by a combined use of simulations and available experimental outcomes (crack gauge recordings) it is possible to circumvent the drawback coming from the lack of exhaustive experimental data.

Further development will address the drawbacks of a unique crack growth law calibration for all the different simultaneously propagating cracks, whereas, when such cracks are located in different process zones (nugget zone, thermo-mechanical affected zone, heat affected zone and base material) a variable calibration for the crack growth law would be necessary to improve accuracy.

References

[1] Rhodes CG, Mahoney MW, Bingel WH, Spurling RA, Bampton CC. Effects of friction stir welding on microstructure of 7075 aluminum. Scripta Mater 1997;36(1):69–75.

[2] Lee CY, Choi DH, Yeon YM, Jung SB. Dissimilar friction stir spot welding of low carbon steel and Al–Mg alloy by formation of IMCs. Sci Technol Weld Joi 2009; 14:216–220.

[3] Carlone P, Palazzo GS. Characterization of TIG and FSW weldings in cast ZE41A magnesium alloy. J Mater Process Technol 2015;215:87–94.

[4] Dressler U, Biallas G, Mercado UA. Friction stir welding of titanium alloy TiAl6V4 to aluminium alloy AA2024-T3, Mater Sci Eng, A 2009;526(1–2):113–117.

[5] Carlone P, Astarita A, Palazzo GS, Paradiso V, Squillace A. Microstructural aspects in Al–Cu dissimilar joining by FSW, Int J Adv Manuf Technol 2015;79:1109–1116.

[6] Moreira PMGP, de Jesus AMP, Ribeiro AS, de Castro PMST. Fatigue crack growth in friction stir welds of 6082-T6 and 6061-T6 aluminium alloys: A comparison, Theor Appl Fract Mec 2008;50:81-91.

[7] Fratini L, Pasta S, Reynolds AP. Fatigue crack growth in 2024-T351 friction stir welded joints: Longitudinal residual stress and microstructural effects, Int J Fatigue 2009;31:495–500.

[8] Bussu G, Irving PE. The role of residual stress and heat affected zone properties on fatigue crack propagation in friction stir welded 2024-T351 aluminum joints, Int J Fatigue 2003;25:77–88.

[9] Tra TH, Okazaki M, Suzuki K. Fatigue crack propagation behavior in friction stir welding of AA6063-T5:

Roles of residual stress and microstructure, Int J Fatigue 2012;43:23-29.

[10] Kumar N, Mishra RS, Baumann JA. Residual Stresses in Friction Stir Welding, Butterworth-Heinemann, 2013.

[11] Dalle Donne C, Biallas G, Ghidini T, Raimbeaux G. Effect of weld imperfection and residual stresses on the fatigue crack propagation in friction stir welded joints, Proceedings of the Second International Conference on Friction Stir Welding, 26-28 June 2000, Gotheburg, Sweden.

[12] Pouget G, Reynolds AP. Residual stress and microstructure effects on fatigue crack growth in AA2050 friction stir welds, Int J Fatigue 2008;30:463–472.

[13] Tra TH, Okazaki M, Suzuki K. Fatigue crack propagation behavior in friction stir welding of AA6063-T5: Roles of residual stress and microstructure, Int J Fatigue 2012;43:23–29.

[14] Živojinović D, Đurđević A, Grbović A, Sedmak A, Rakin M. Numerical Modelling of Crack Propagation in Friction Stir Welded Joint Made of Aluminium Alloy. Proc Mater Sci 2014;3:1330–1335.

[15] Zadeh M, Ali A, Golestaneh AF, Sahari BB. Three dimensional simulation of fatigue crack growth in friction stir welded joints of 2024-t351 Al alloy, J Sci Ind Res 2009;68:775-82.

[16] Citarella R, Carlone P, Lepore M, Palazzo GS. Numerical–experimental crack growth analysis in AA2024-T3 FSWed butt joints, Adv Eng Softw 2015;80:47–57.

[17] Carlone P, Citarella R, Lepore M, Palazzo GS. A FEM-DBEM investigation of the influence of process parameters on crack growth in aluminum friction stir welded butt joints. Int J Mater Form 2015;8(4): 591-599.

[18] Citarella R, Carlone P, Sepe R, Lepore M. DBEM Multiple Crack Propagation in Friction Stir Welded Aluminium Joints, Eng Fract Mech, accepted for publication.

[19] Citarella R, Carlone P, Sepe R, Lepore M. DBEM Crack Propagation in Friction Stir Welded Aluminium Joints, Adv Eng Softw, accepted for publication, DOI 10.1016/j.advengsoft.2015.12.002.

[20] Sonne MR, Tutum CC, Hattel JH, Simar A, de Meester B. The effect of hardening laws and thermal softening on modeling residual stresses in FSW of aluminum alloy 2024-T3, J Mater Process Tech 2013;213:477– 486.

[21] Schmidt H, Hattel JH. Thermal modelling of friction stir welding, Scripta Mater 2008;58:332–337.

[22] Myhr OR, Grong O. Process modeling applied to 6082-T6 aluminum weldments. Part 1: Reaction kinetics. Part 2: Applications of model, Acta Metal 1991;39:2693–2708.

[23] Richards DG, Pragnell PB, Williams SW, Withers PJ. Global mechanical tensioning for the management of residual stresses in welds, Mater Sci Eng A 2008;489:351–362.

[24] Sadananda K, Vasudevan AK. Short crack growth and internal stresses. Int. J. Fatigue 1997; 19: 99-108.

[25] Citarella R, Cricrì G. A two-parameter model for crack growth simulation by combined FEM-DBEM approach, Adv Eng Softw 2009;40:363-373.

[26] Sonne MR, Carlone P, Palazzo GS, Hattel JH. Numerical modeling of AA2024-T3 friction stir welding process for residual stress evaluation, including softening effects, Key Eng Mater 2014;611-612:1675-1682.

[27] Richter-Trummer V, Suzano E, Beltrão M, Roos A, dos Santos JF, de Castro PMST. Influence of the FSW clamping force on the final distortion and residual stress field, Mater Sci Eng, A, 2012;538:81–88.

[28] Sonne MR, Carlone P, Citarella R, Hattel JH. Integrated FEM-DBEM simulation of crack propagation in AA2024-T3 FSW butt joints considering manufacturing effects, Key Eng Mater 2015;651-653:877-882.

[29] Prime MB. Cross-sectional mapping of residual stresses by measuring the surface contour after a cut, J Eng Mater-T 2001;123:162-168.

[30] Carlone P, Palazzo GS. Longitudinal Residual Stress Analysis in AA2024-T3 Friction Stir Welding. Open Mech Eng J 2013;7:18-26.

[31] BEASY V10r14, Documentation, C.M. BEASY Ltd; 2011.

[32] Rigby RH, Aliabadi MH. Decomposition of the mixed-mode J-integral – revisited. Int J Solids Struct 1998; 35(17): 2073–99.

Figure1
Click here to download high resolution image

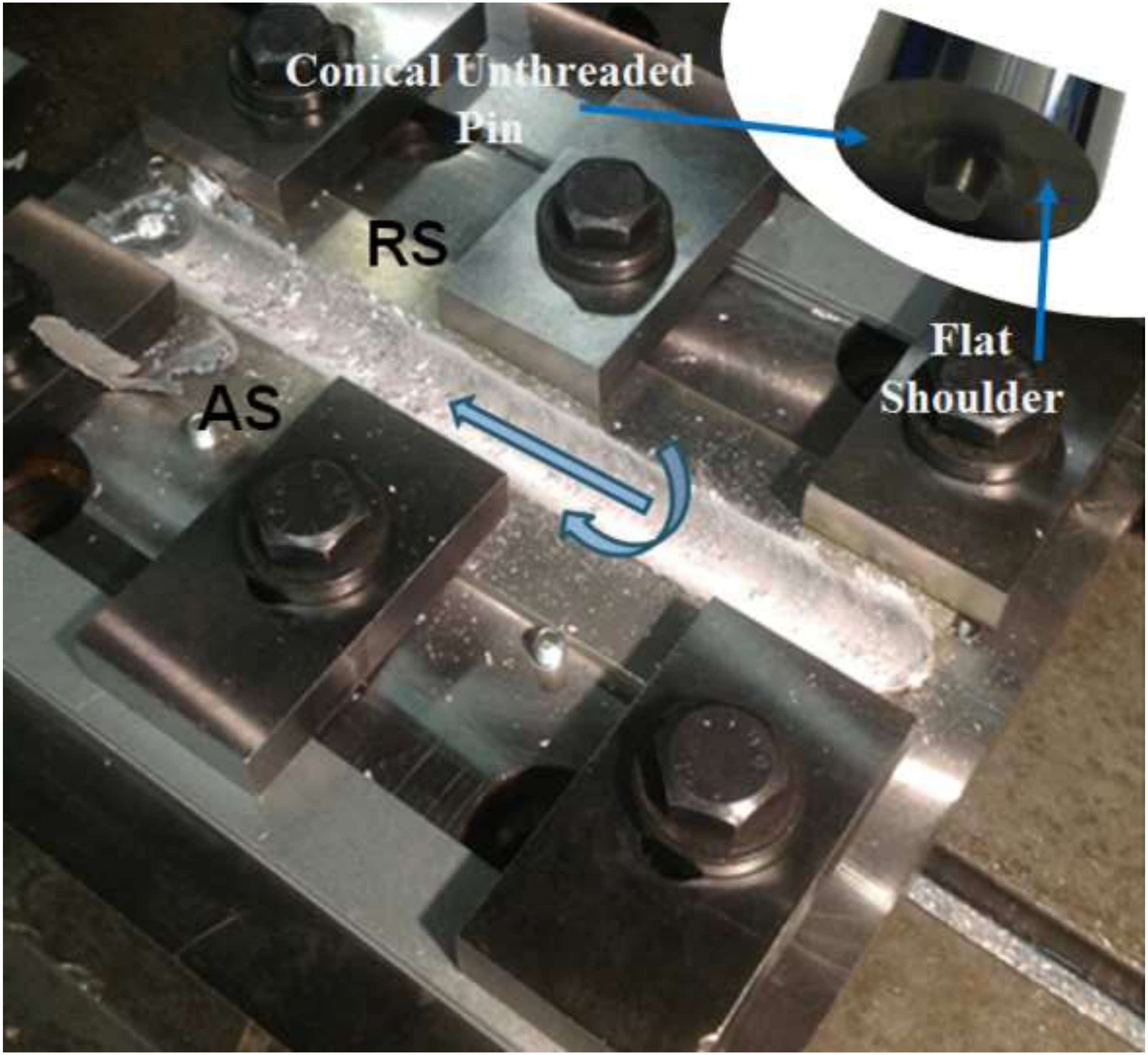

Figure2

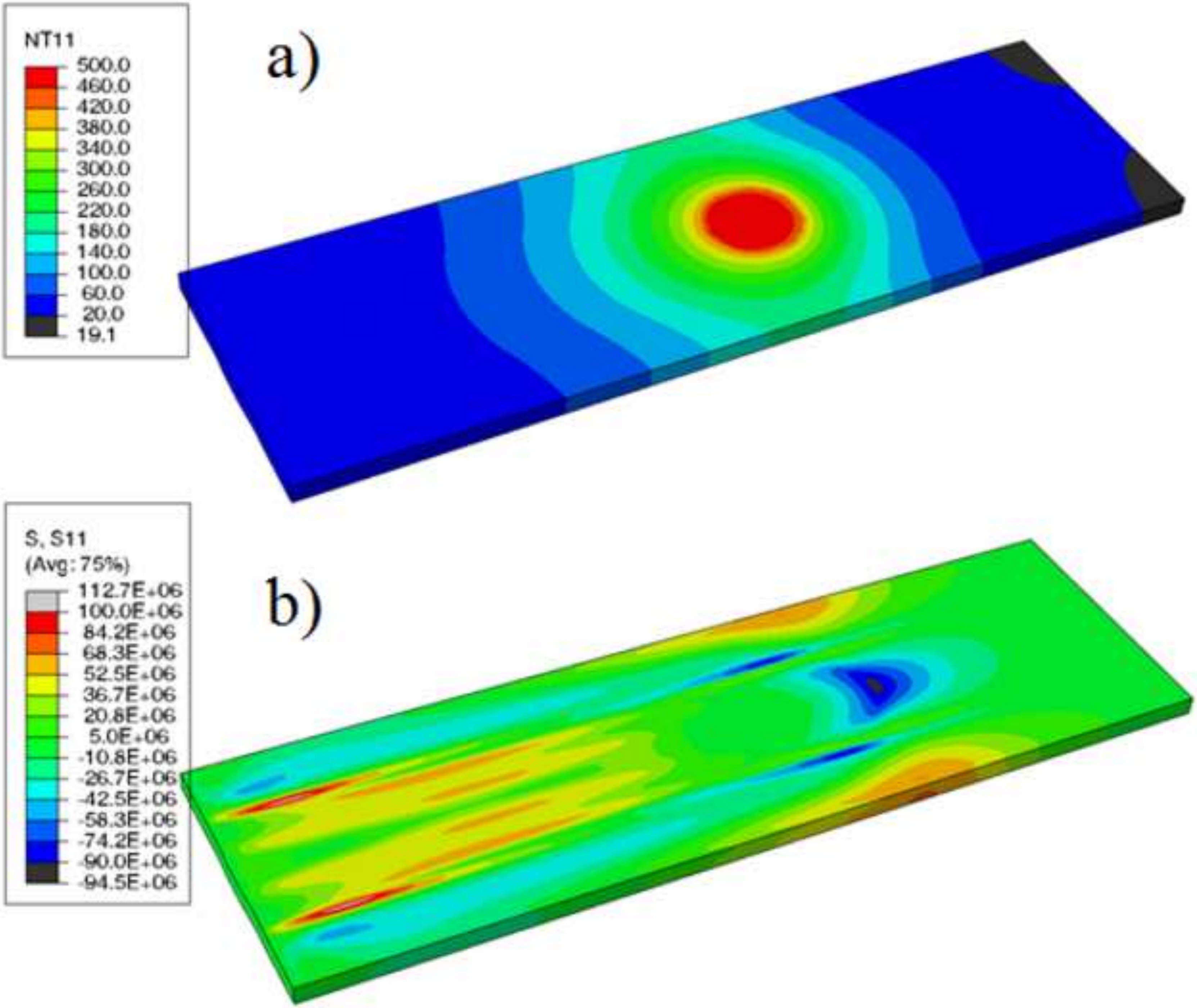
NT11
500.0
460.0
420.0
380.0
340.0
300.0
260.0
220.0
180.0
140.0
100.0
60.0
20.0
19.1
a)
S, S11
(Avg: 75%)
112.7E+06
100.0E+06
84.2E+06
68.3E+06
52.5E+06
36.7E+06
20.8E+06
5.0E+06
-10.8E+06
-26.7E+06
-42.5E+06
-58.3E+06
-74.2E+06
-90.0E+06
-94.5E+06
b)

Figure3

Click here to download high resolution image

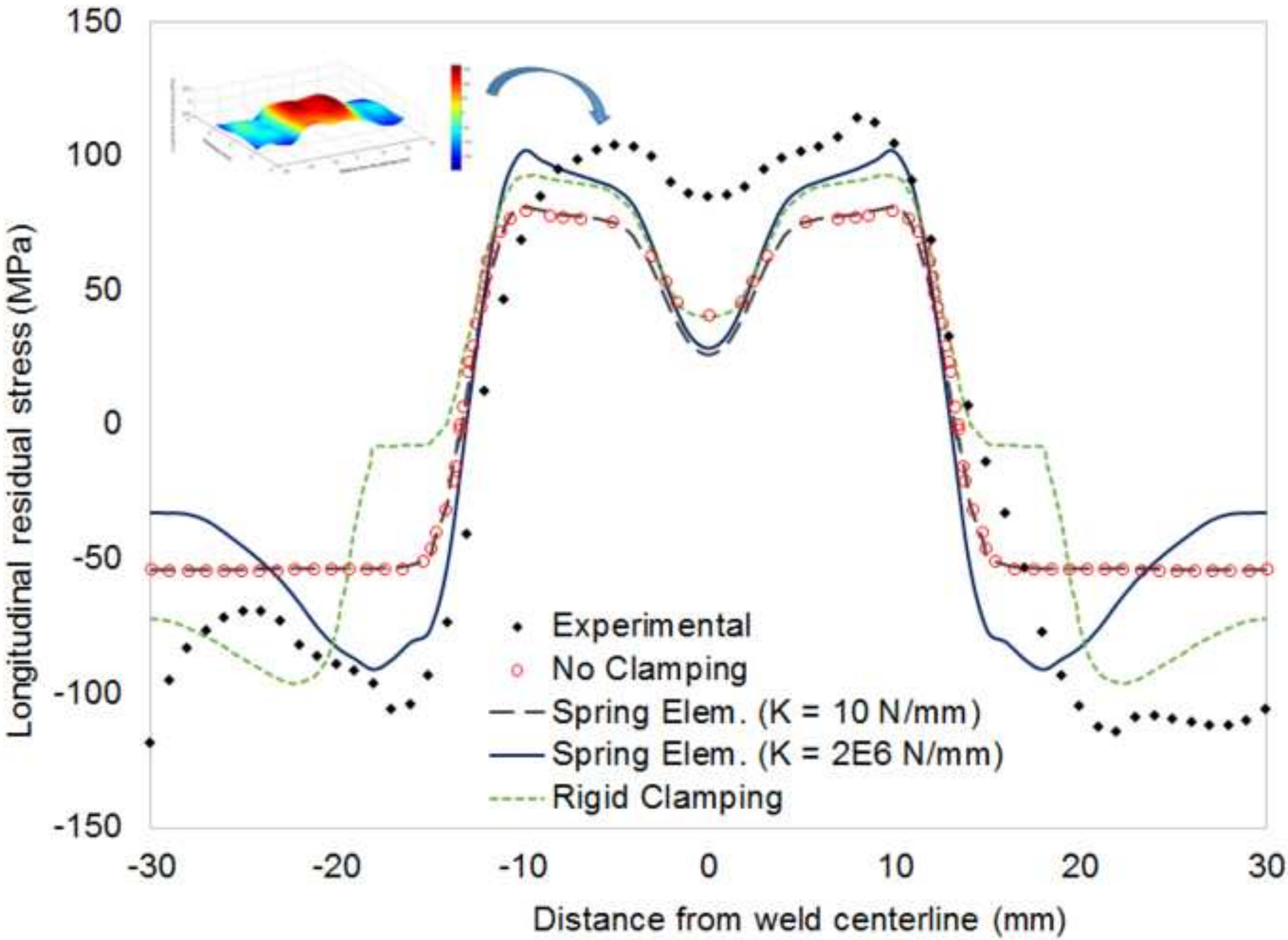

Figure4

Click here to download high resolution image

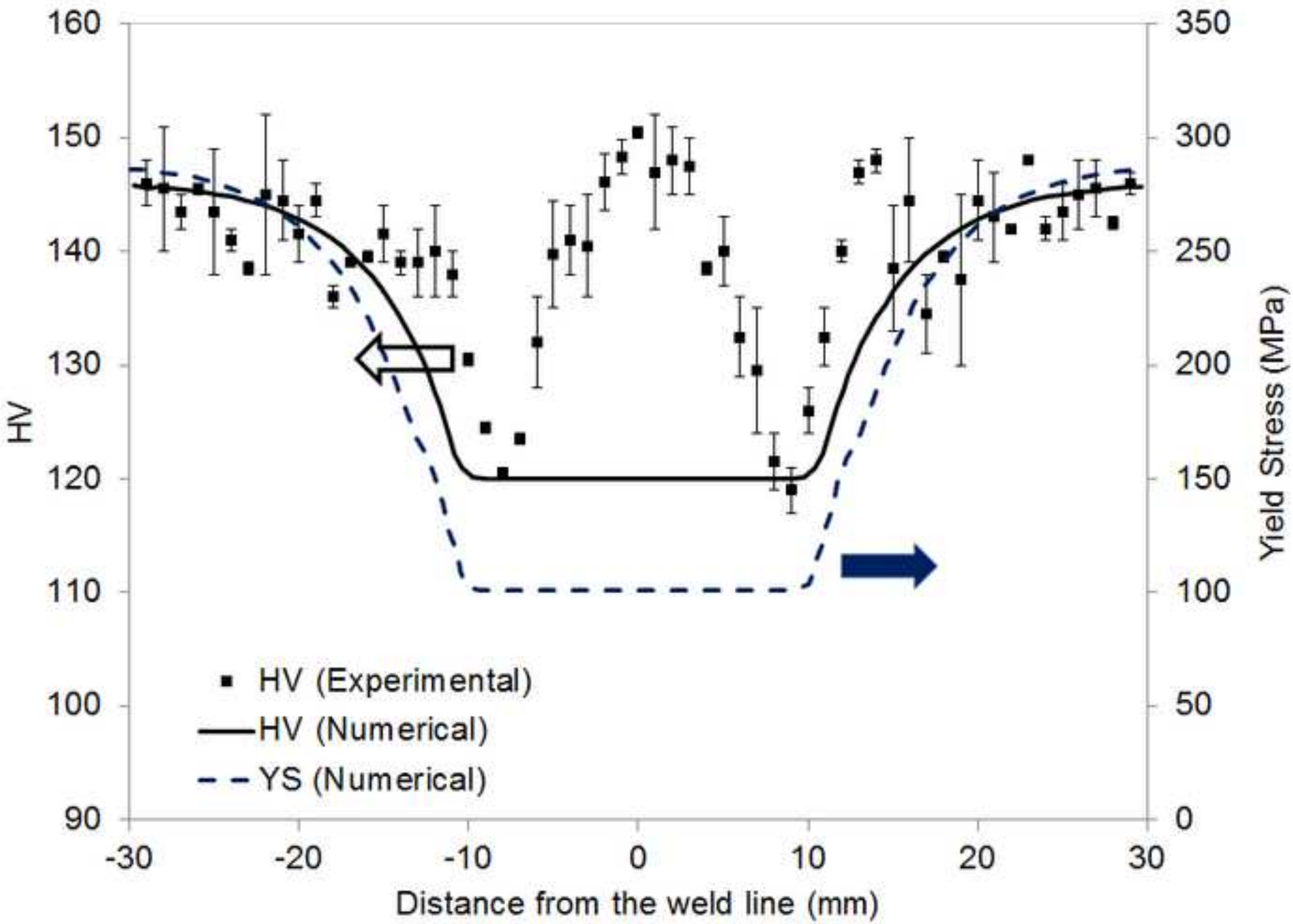

Figure5

Click here to download high resolution image

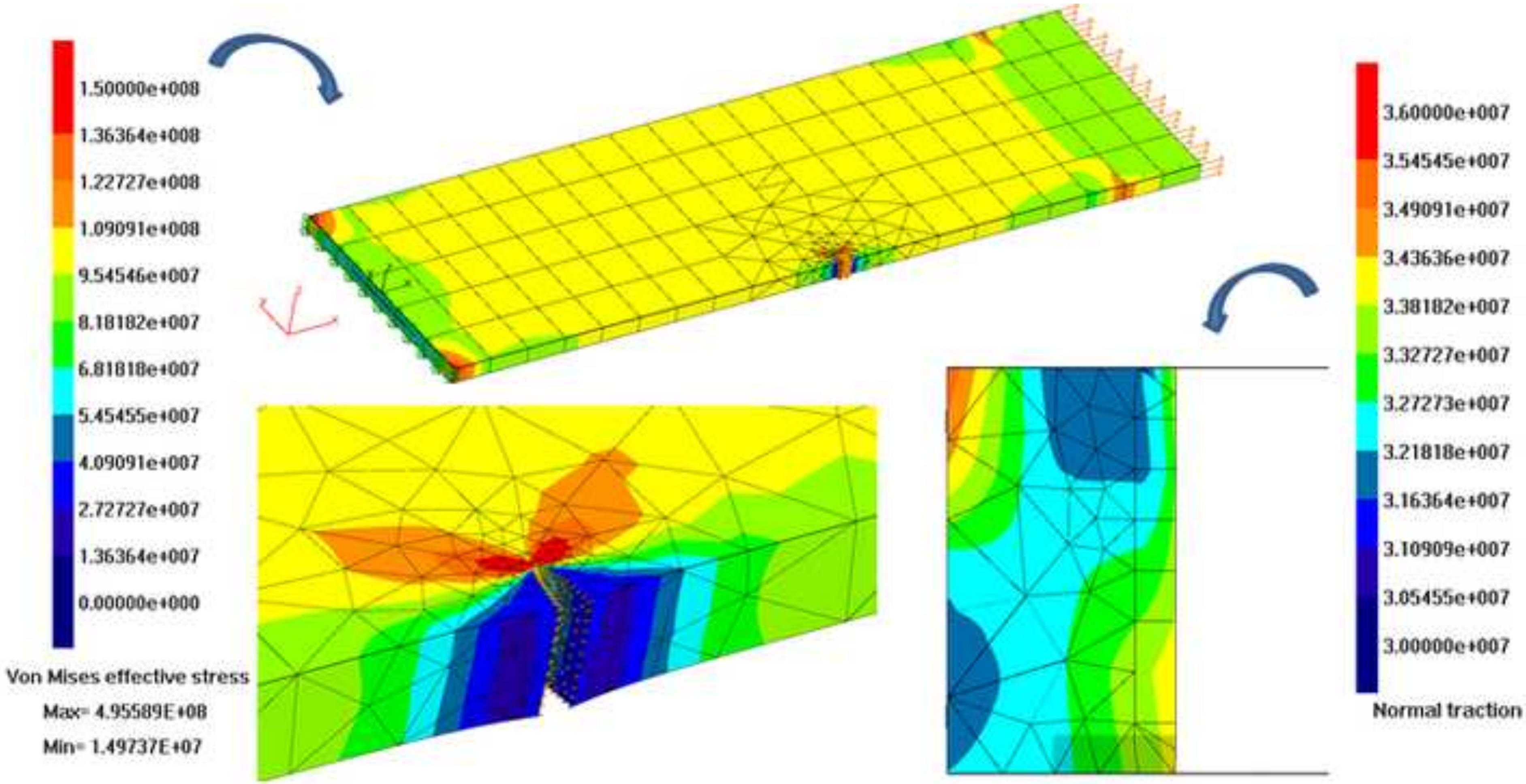

Figure6
Click here to download high resolution image

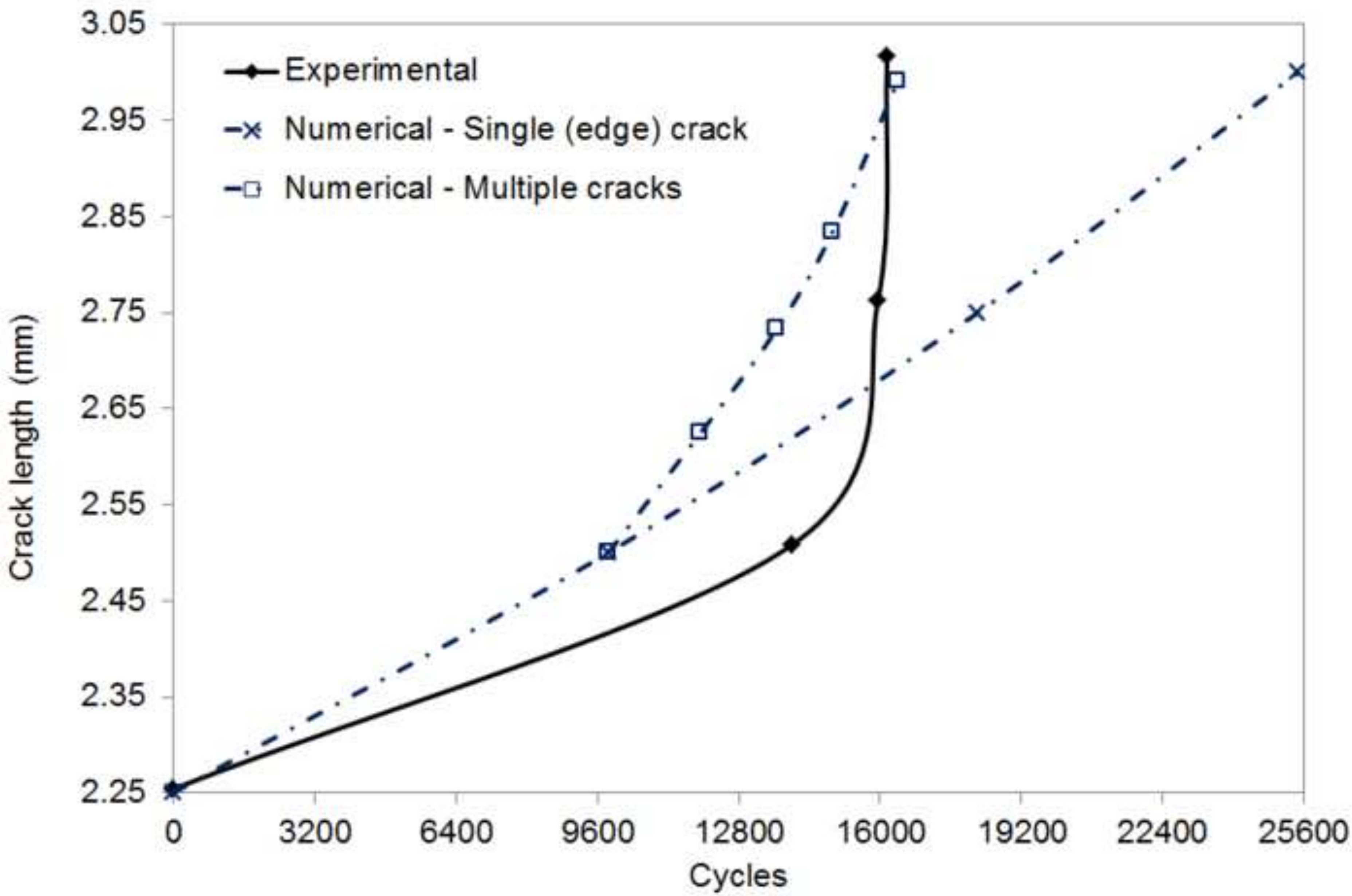

Figure7

Click here to download high resolution image

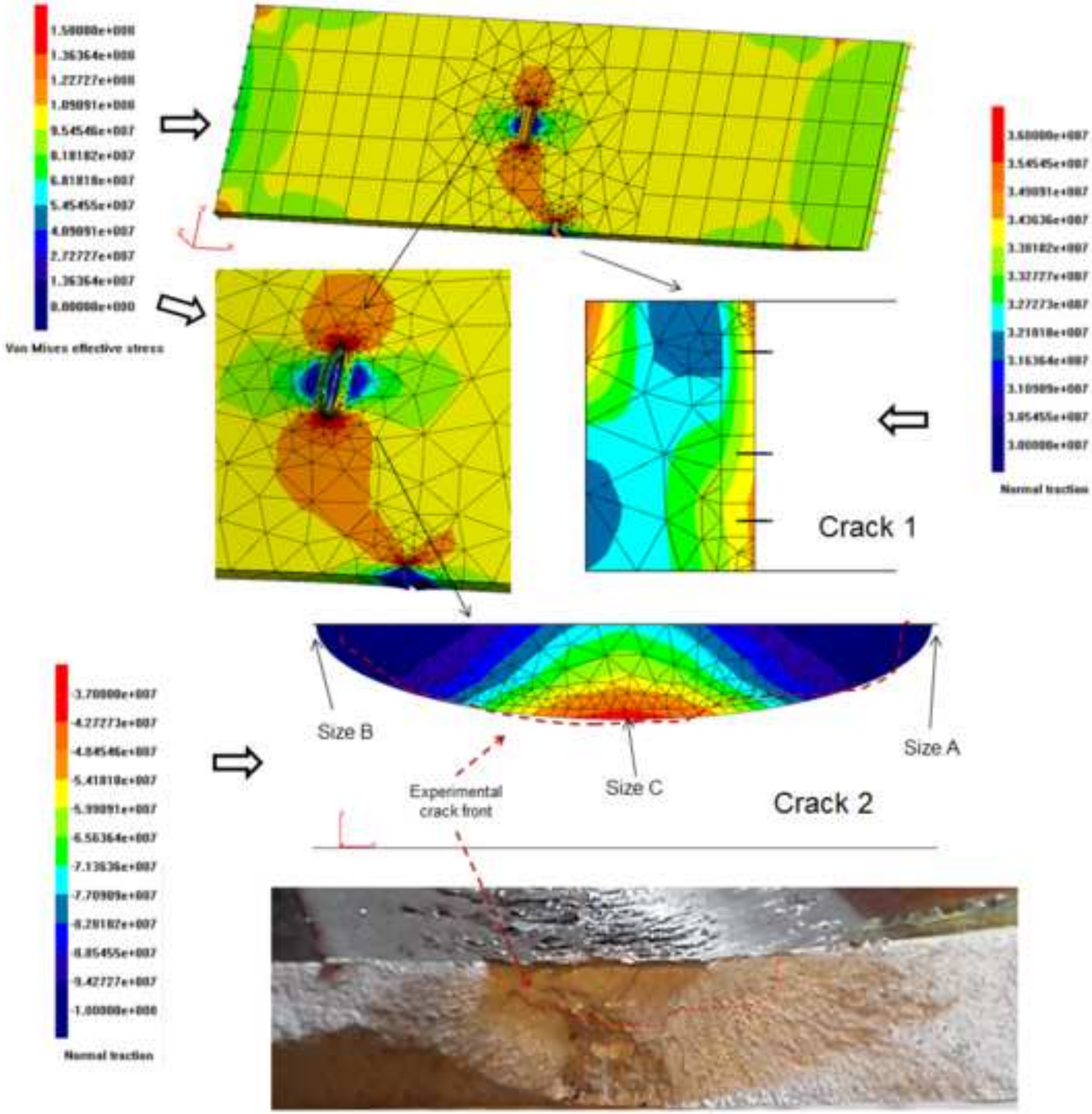

Figure8

Click here to download high resolution image

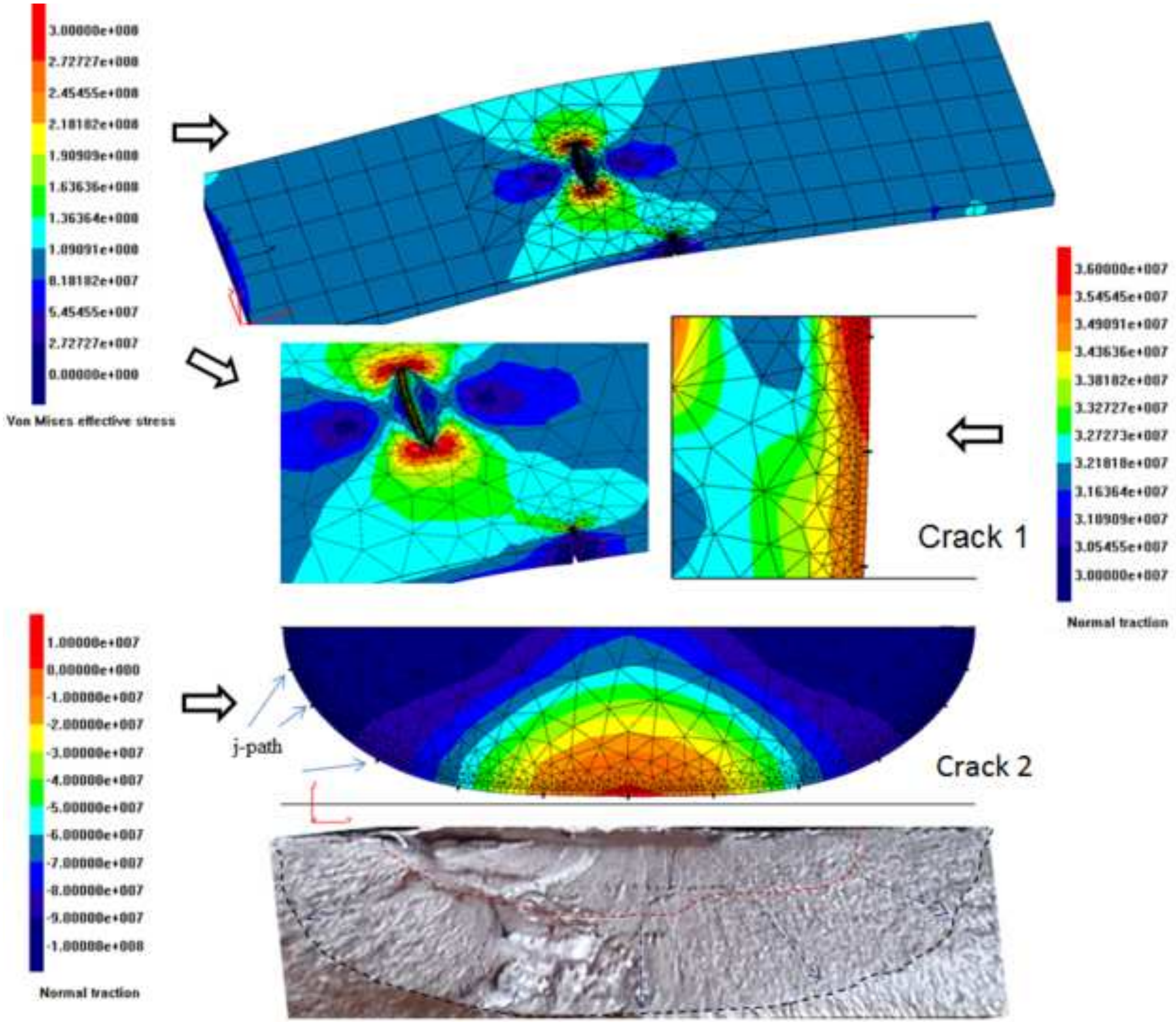

Figure9

Click here to download high resolution image

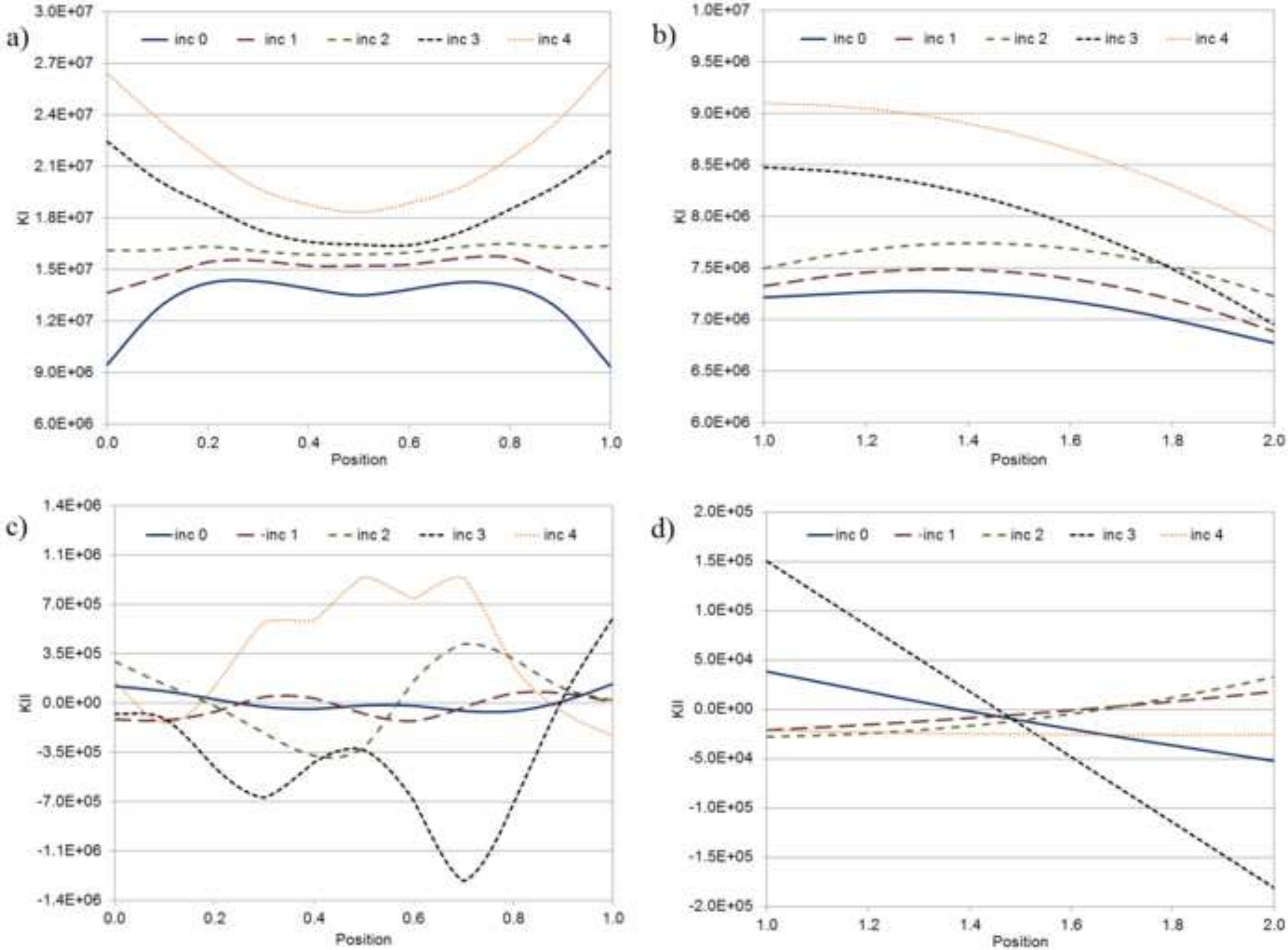

Figure10

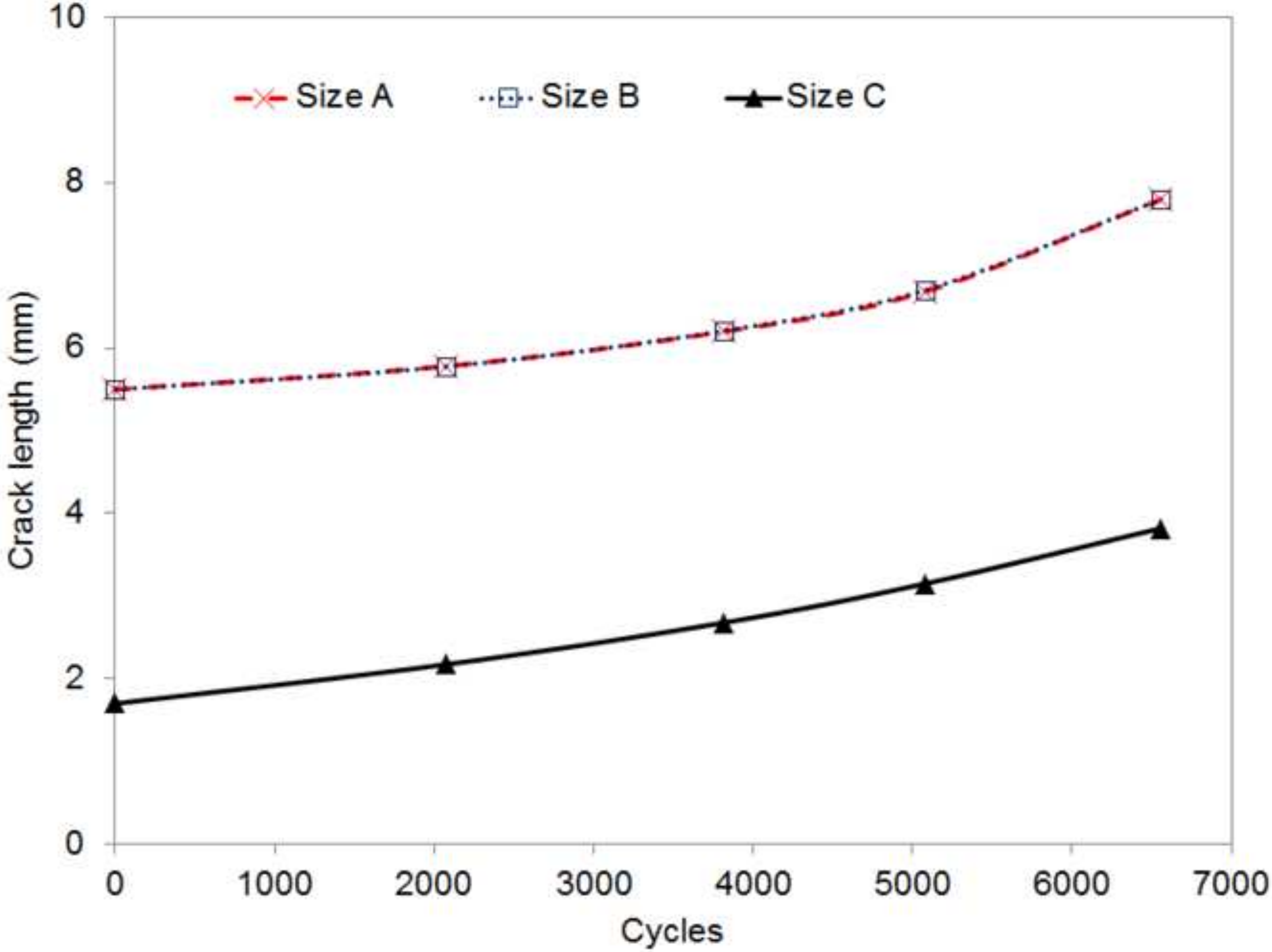
Size A
Size B
Size C
Crack length (mm)
Cycles
0
2
4
6
8
10
0
1000
2000
3000
4000
5000
6000
7000